Experimental and Numerical Investigation of Ballistic Impact Response of Polymethylmetacrylate

Youngjoon Jeon
Khalid M. Mosalam

Department of Civil and Environmental Engineering
University of California, Berkeley, California

Experimental and Numerical Investigation of Ballistic Impact Response of Polymethylmetacrylate

Youngjoon Jeon

Khalid M. Mosalam

Department of Civil and Environmental Engineering
University of California, Berkeley, California

Abstract

For understanding characteristics of Polymethylmetacrylate (PMMA) under impact, the damage behavior of PMMA plates with various thicknesses (1.5 to 6.0 mm) subjected to ballistic impacts with various velocities (63 to 180 m/s) is experimentally investigated using a specialized testing apparatus. Moreover, numerical simulations using the Finite Element Method (FEM) are conducted for the corresponding experimentally studied cases. Ductile response and brittle tensile failure behavior are considered in the FEM to describe the nonlinear response and the failure mode of the PMMA plates. The numerical simulations effectively describe the shape of cracks and perforations of the PMMA plates for all studied 25 cases verifying the validity of the numerical model. Although the PMMA plates are generally brittle in the selected range of impact velocity, it is found that these plates exhibit ductile behavior under low-velocity impacts. Moreover, the numerical simulations imply that the kinetic energy loss of the projectile is linearly dependent on the plate-thickness while the impact velocity hardly affects this loss. This behavior obtained experimentally and numerically illustrates the usefulness of the PMMA material for the use as a protective layer in many applications involving ballistic (high velocity) impacts.

Keywords: Ballistic impact, Brittle behavior, Ductile response, Failure mode, FEM, PMMA.

Acknowledgements and Disclaimer

Contents

List of Tables

List of Figures

1   Introduction[1]

Polymethyl methacrylate (PMMA) is one of the most used transparent polymeric materials, which is commercially known as acrylic and is also called Plexiglas by the trade name. The material is characterized by lightness, high strength to density ratio, and Ultraviolet (UV) & heat resistances, and high transparency. Especially, due to its advantages in low-cost, high strength-density ratio, and transparency, the material can be a substitute for glass material in many applications such as construction (Pawar 2016), and exterior layer of Photovoltaic (PV) panels (Kajisa et al. 2014; Martins et al. 2018; Zahid et al. 2021). Moreover, the military applications of PMMA include its use as transparent armor in face shields, blast shields, vehicle vision blocks, and aircraft (Patel et al. 2006), and eye protection gears (Hsieh J. et al. 2004).

The capacity and damage behavior of PMMA need to be characterized for the applications as a protective material under diverse loading cases. Even though the impact behavior of PMMA material has been studied for decades from numerous research, most of these past studies had a limited scope, which focused on specific loading conditions of one or two damage modes, e.g., uniaxial tensile load or shear/compression combined loads (Zhou et al. 2013; Zhang et al. 2016). Moreover, the mechanical properties have been studied under static or quasi-static loading conditions, which are usually too idealized in experimental settings. Thus, more practical loading conditions should be considered to expand the application of the PMMA material with data describing the global and dynamic response of this material.

Various loading and impact conditions have been conducted and presented to study the materials' damage response. While the Hopkinson experimental technique (Jiang and Vecchio 2009; Gama et al. 2004) is a mainstream method for studying impact-dynamic properties of materials, numerous studies in the literature have successfully used the ballistic impact technique to investigate the impact response of various materials, including polymers like PMMA. Among different loading cases, ballistic impact is chosen for this study as it is viable within the available laboratory setting, which enables targeting different levels of loading for each impact and can offer a more general loading conditions for the failure response of the PMMA material under complex modes. Ballistic impact load is widely used to study the material properties, especially to find the damage behavior of materials (Dong et al. 2012; Petrudi et al. 2020; Ogihara et al. 1998). The damage behavior of materials is described by investigating the size of perforation holes, crack patterns, and ballistic limit which are determined by the velocity and the kinetic energy conveyed from ballistic impact (Kueh and Siaw 2021; Ogihara, Ishigure, and Kobayashi 1998; Pereira, Weerheijm, and Sluys 2018).

This research aims to gain fundamental insight on the impact response and failure behavior of PMMA plates from the point of view of energy conversion trends under ballistic impact

considering variations in the plate-thickness and projectile velocity. While the mechanical properties of PMMA have been studied in previous research, they often address specific types of impact loadings, such as static loadings, in-plane loading, or low-speed impact, e.g., free-drop. In this study, we extend the scope by examining the impact response under more practical conditions. One adopted numerical model from the literature (Dorogoy et al. 2010) is verified using this experimental/numerical investigation including experimental study and numerical simulation using the Finite Element Method (FEM). ABAQUS/EXPLICIT FEM package performs various impact simulations addressing loading conditions on blast (Hanifehzadeh et al. 2019), collision (Kueh and Siaw 2021), and static loads (Gee et al. 2020), etc. Furthermore, comparative results from the verified numerical model are interpreted to describe the impact behavior obtained using the FEM. Our study not only contributes to the understanding of PMMA's behavior under ballistic impacts but also provides insights for designing and optimizing protective glazing systems in buildings, ensuring their resilience against potential ballistic threats.

2 Ballistic Impact Experiment

2.1 Experimental Setup

A projectile-launching system was utilized to conduct the ballistic impact-experiment on Plexiglass plates. Fig. 2.1 schematically describes the overall system of the shooting equipment. A Nitrogen tank connected with a pressure vessel provides the required pressure in the chamber. A projectile (bullet) is inserted in the front end of the barrel. The pressurized Nitrogen gas being controlled by two regulating valves propels the bullet. With an electronic signal transmitted to the device, using the fire button, the bullet in the chamber is released and passes through the barrel. Two laser points and a receptor are installed between the end of the barrel and the target to measure the time interval spent for a projectile to pass these two points aligned with lasers. The initial velocity can be calculated from the time interval received by a light-sensor (receptor) which responds once the light from the lasers is blocked due to a projectile. Throughout the experiments, it is assumed that the initial velocity remained constant up to the moment of impact within the designed range of impact velocities. This assumption of the test setup is reasonable considering the consistently centralized penetration hole observed in our experiments, indicating that the bullets follow their original path despite the 0.9 m gap between the end of the barrel and the target. It is noted that this gap is essential to ensure unobstructed visualization for precise deformation and damage measurements, which are crucial for our study employing Digital Image Correlation (DIC). A digital camera was installed at 30 cm distance from each target to conduct 2-Dimensional Digital Image Correlation (2D-DIC) to determine the in-plane deformation of the damaged test plates (Pan 2018). It is noted that the 2D-DIC method within the current scope of study provides preliminary experimental data which should be expanded in future studies by conducting 3D-DIC where not only in-plane, but also out-of-plane deformation and damage behavior can be tracked.

The PMMA plates, extruded acrylic Plexiglass (TAP PLASTICS®), were prepared with 5 values of thickness from 1.5 mm to 6.0 mm for the dimension of 125 mm $\times$ 175 mm, Fig. 2.2(a). PMMA can be commonly manufactured by either extrusion or cast where molten PMMA is placed into a metal dye being extruded by pressure or being solidified, respectively. Between the two types of manufactured PMMA plates, i.e., extruded by pressure and chemically cast, the extruded PMMA was selected in this study to determine the impact resistance and to be consistent with the numerical model where the material properties were obtained from references of extruded PMMA. Considering that both end-sides were clamped by aluminum plates, the plane-dimensions of each plate were determined to have 125 mm $\times$ 125 mm as the effective area for testing. Projectiles made of steel material were 25.4 mm long with 12.7 mm diameter as shown in Fig. 2.2(b).
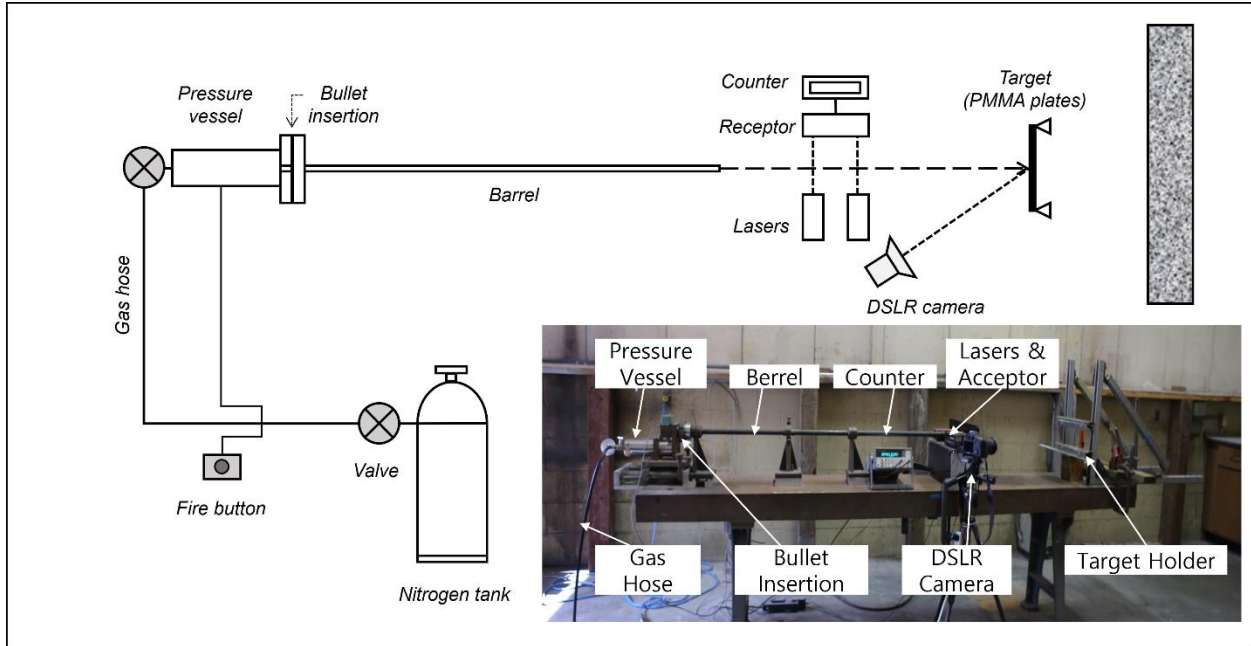
Figure 2.1 **A schematic diagram and inserted photograph of the projectile-launching system.**

(a)   (b)
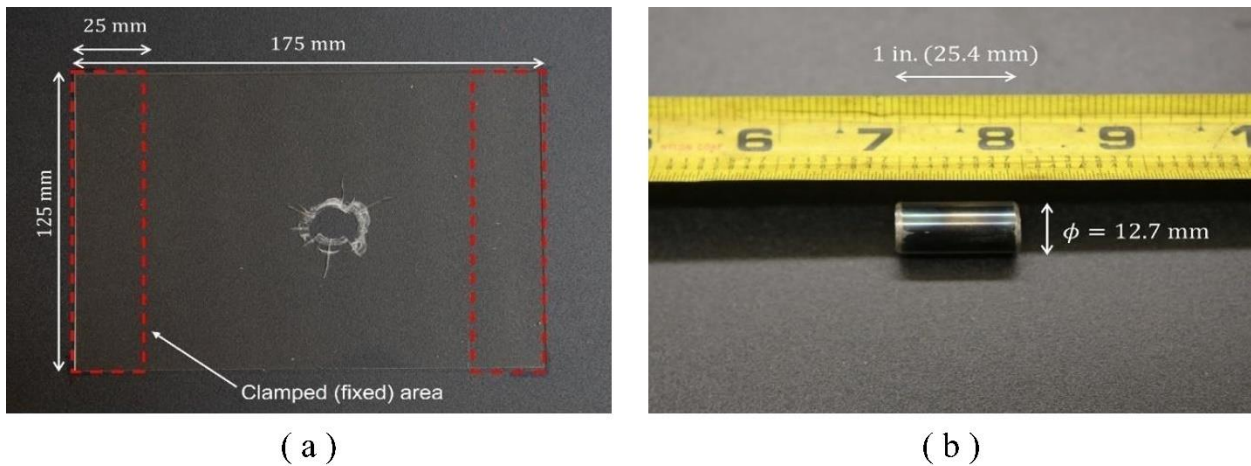
Figure 2.2 **Dimensions of the PMMA plate and the cylindrical projectile (bullet).**

2.2 Execution of the Experiments

The experiments using the gas-gun were conducted on plates with 5-thickness cases and 5 variant pressure settings, repeated twice for speckled plates (used for the purposes of DIC (Pan, 2018))

and non-speckled (transparent) plates. The Design of Experiment (DoE) was employed to systematically vary the input parameters and ranges of the experimental scheme to understand their influence on the experimental outcome. Appropriate ranges of velocity and plate thickness were established to study the varying response from the simple penetration to the severe fracturing of the plate for each parameter based on their expected influence and practical constraints (Ogihara et al. 1998). The range of impact velocities 60 m/s to 180 m/s was designed for the purpose of observing both ductile and brittle damage behavior. The range of velocities aligns with prior studies which focused on brittleness in the higher velocities (Sarva et al. 2006), and examined mixed failure modes without perforation behavior below drop impact velocity, the lower shooting velocity (Tekalur et al. 2010). Moreover, the variation in plate-thickness between 1.5 to 6.0 mm aimed to explore the damage behavior during perforation among ballistic phases described in (Ogihara et al. 1998). Within the range of velocities and the targets' thickness, the determination of the number of experimental cases, 25 in total, was determined to strike a balance between statistical significance and practical feasibility. Initial velocities, $v_i = \frac{L}{\Delta t}$, were calculated from the determined different time intervals, Δt, and the fixed distance, $L = 63.5$ mm, between the two lasers, Fig. 2.1. The impact velocities varied between 57.62 m/s to 182.00 m/s (underlined in Table 2.1) depending on the pressure exerted into the system. Prior to testing of the PMMA plates, the relationship between pressure and velocity was studied to determine the bullet-velocity variation. Fig. 2.3 shows the determined pressure-velocity relationship. From this figure, five levels of pressure were set for velocity variation for each shooting. It is observed that the bullet-velocity is nonlinearly increasing with the increase of the controlled pressure. Table 2.1 provides the velocity variation used for each shooting and the corresponding PMMA plate thickness cases, h_j ($j = 1 \rightarrow$ 5). Note that the last two columns in Table 2.1 represent the average projectile velocity (μ_v) for each of the five considered pressure settings ($i = 1 \rightarrow 5$) computed from the five different cases of the studied plate thicknesses and the corresponding Coefficient of Variation (CoV). It is noted that the variation of the initial velocity due to the inherent randomness of the load application is small (i.e., less than 8.2% CoV) from one PMMA plate thickness case to another. Images of the plate surface were taken before and after each impact in *.raw* file format. The noise originating from the displacement of the camera was minimized using a remote control to take images, which prevents dislocation caused by touching the camera body. The acquired images were converted into *.tiff* format to save images into vector format to be analyzed by the DIC software *OpteCAL* (Barthes 2022).
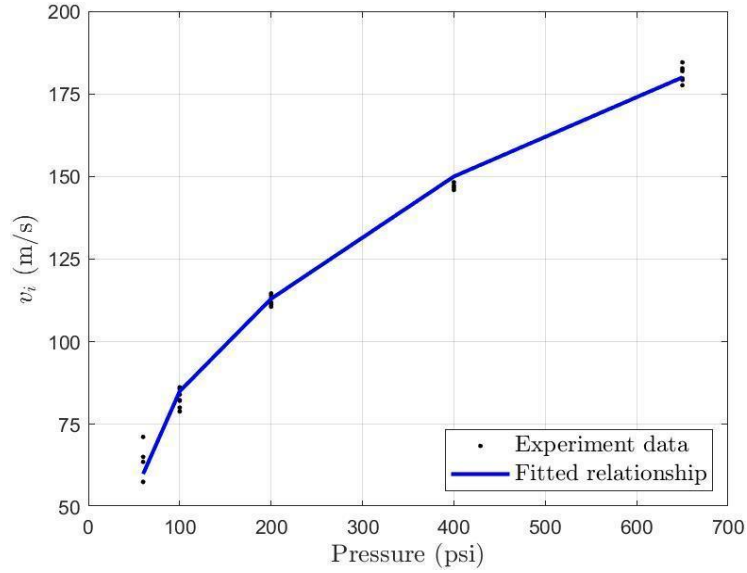
Figure 2.3   Initial projectile velocity from the controlled gas-pressure [100 psi = 0.6895 MPa]

Table 2.1   Initial pressure values and measured velocities

i	Pressure (psi) [MPa]	Initial velocity (v_i) (m/s) for different h_j (mm) cases					μ_v (m/s)	CoV (%)
		$h_1 = 1.5$	$h_2 = 2.5$	$h_3 = 3.0$	$h_4 = 4.5$	$h_5 = 6.0$		
1	60 [0.414]	<u>57.62</u>	63.65	71.20	65.16	57.57	**63.04**	**8.11**
2	100 [0.690]	80.08	78.91	85.68	85.93	84.04	**82.93**	**3.50**
3	200 [1.379]	111.93	111.40	110.61	114.00	114.64	**112.52**	**1.37**
4	400 [2.758]	147.30	148.26	146.69	145.94	146.48	**146.93**	**0.54**
5	650 [4.137]	<u>182.00</u>	179.23	177.62	179.43	181.90	**180.04**	**0.94**

2.3   Experimental Results

The speckled PMMA plates after ballistic impact are shown in an array in Fig. 2.4 for all 25 studied cases. The corresponding numerical values for the five plate-thickness cases (h_1 to h_5) and five projectile-speed values (v_1 to v_5) are listed in Table 2.2. The typical velocities are selected based on the average values (μ_v) in Table 2.1. All shootings for each plate thickness case corresponded

to plates fully penetrated by the targets, exceeding their ballistic limit. It is observed that the plates experienced clear variations in the crack patterns depending on the thickness and impact velocity. The perforation hole size of each plate decreased with the increase of the impact-velocity for a fixed plate thickness. The variations in the length and the pattern of the cracks in each thickness case for different impact-velocity show similar trends. The shape of the perforation holes becomes closer to circles, being more like the shape of the bullet, with the higher-velocity shooting. The variation in the crack patterns with the increase of the plate-thickness is also clearly observed. The plate with larger thickness had in-plane cracks propagating further and sometimes reaching the edges of the plate. The white zone around the perforation hole, clearly shown in Fig. 2.2(a), is formed due to the damage exerted through the thickness on thick plates creating a conical shaped hole.

The above observations are also supported by the DIC results of the first principal strain fields on the PMMA plate surfaces facing the incoming projectile after impacts. Fig. 2.5(a) compares these principal strain fields of the PMMA plates with different thickness for $v_3 = 113$ m/s where the damage zone formed around each perforation hole is subjected to tensile strains. The damage area is localized around the propagated cracks rather than showing globally distributed contours. Moreover, the area of the tensile-damage zone expands with the increase of the plate thickness. However, this variation of the tensile-damage zones is much less pronounced in Fig. 2.5(b), which compares plates impacted by different projectile velocities for $h_3 = 3.0$ mm. The comparison between the two sets of results indicates that the increase of the plate thickness results in more global deformation pattern of the test PMMA plate. On the other hand, the velocity variables of the projectile have less effect on the deformation pattern. This observation is further evaluated in the following section using numerical studies based on the energy absorption history.

Table 2.2   **PMMA plate thickness and the projectile-velocities**

i	h_i (mm)	v_i (m/s)
1	1.5	63
2	2.5	83
3	3.0	113
4	4.5	147
5	6.0	180
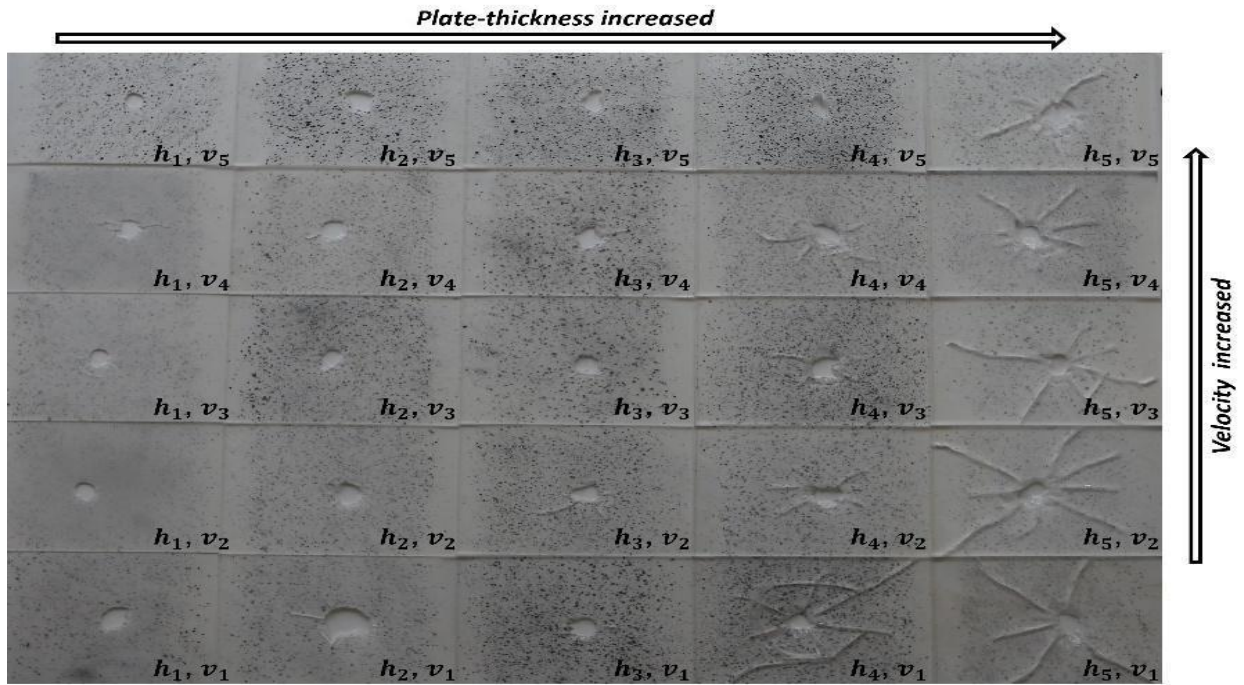
Figure 2.4   Speckled plates after ballistic impacts
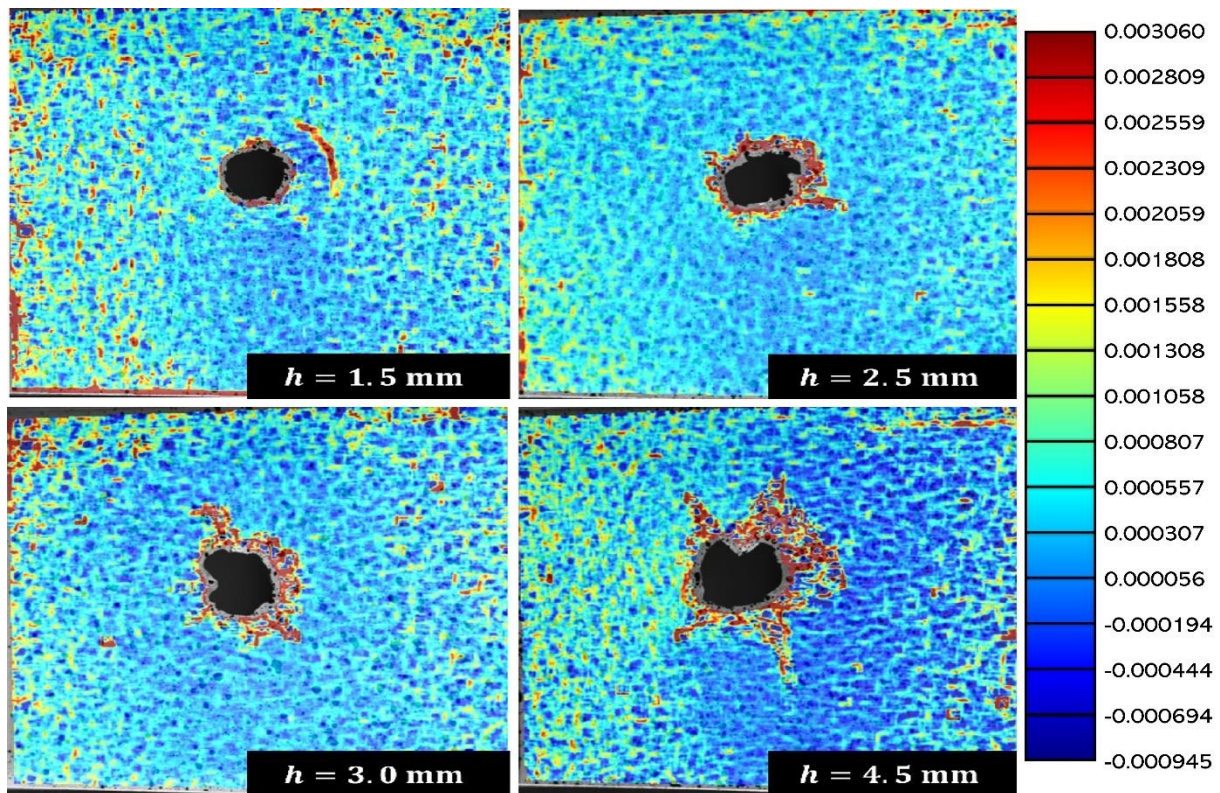
Figure 2.5   DIC first principal strain field of the selected PMMA plates

3   Numerical Simulations

The simulation of ballistic impact behavior of the PMMA plates was executed using the commercial software ABAQUS/CAE (*CAE Abaqus* 2009) and ABAQUS/Explicit (Hibbit and Karlson 1998). Five models for plates of different thicknesses were developed, and they were subjected to different projectile-velocity settings. Five velocity cases were set based on the velocities measured in the experiments. Numerical values for the five thickness models (h_1 to h_5) and five projectile velocities (v_1 to v_5) follow the predefined values in Table 2.2.

3.1   Geometry and Assembly

Each model using the FEM was comprised of three parts: PMMA plate, projectile, and boundary (target holder) aluminum plates, Fig. 3.1. The dimensions of these parts were the same as those of the test specimens. The PMMA plate was discretized with a 75 mm-diameter central circle as shown in Fig. 3.1. This configuration was useful to define irregular shape and position of the finite elements so that cracks can be propagated in arbitrary directions. This agreed with the fact that the projectile impacted on the center of the PMMA plate, leading to subsequent contact to the plate surface.
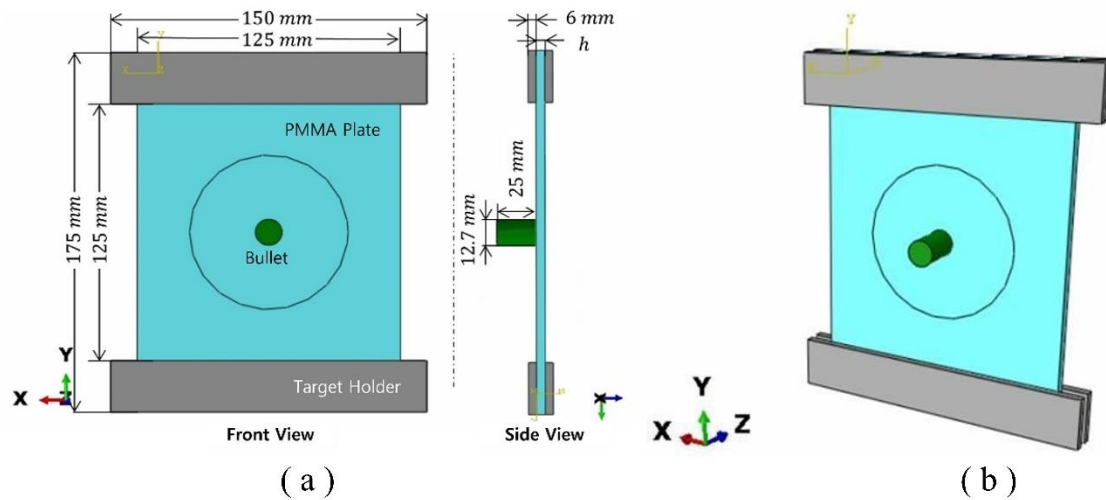
Figure 3.1   PMMA plate and bullet model in ABAQUS/CAE.

Table 3.1   Material properties used in the numerical model

Material	Young's modulus (GPa)	Poison's ratio	Material density (kg/m^3)
PMMA	5.76	0.42	1,190
Steel	210	0.30	7,800
Aluminum	70	0.33	2,600

3.2   Material Properties

The mechanical properties of PMMA, steel, and aluminum were selected as listed in Table 3.1 (Rittel and Brill 2008; Rittel and Dorogoy 2008; Scari et al. 2014; Dorogoy and Rittel 2014; Bless et al. 2018). Since the aluminum plates and the steel projectiles were sufficiently rigid relative to the PMMA plate, the elastic properties were the only ones defined without considering any failure behavior. On the other hand, the properties of the PMMA plates were specified to describe their full behavior. The plastic behavior and the corresponding hardening law of PMMA were specified according to (Rittel and Brill 2008; Dorogoy et al. 2010). To account for the rate dependent characteristics of PMMA, the stress-strain relationship corresponding to strain rate of 40,000 s^{-1} was considered, which was judged to be a reasonable estimate under the expected high-strain rate effect of the conducted high-speed impact study. It is noted that strain rates within the broad range of 4,000 to 40,000 s^{-1} did not affect the stress-strain relationship of PMMA (Rittel and Brill 2008; Dorogoy et al. 2010). However, the dependency of PMMA on temperature and pressure was not considered in this study since the effect from those factors were expected to be negligible in the current setting of the conducted experiments.

3.3   Failure Criteria and Damage Behavior of PMMA

The damage behavior and criteria adopted in the FEM considered the findings from previous studies (Rittel and Brill 2008; Rittel and Dorogoy 2008; Dorogoy et al. 2010). Both ductility and brittleness of the PMMA material were used for accurate representation of the plates under the existing loading and boundary conditions.

The ductility properties were assigned to the model following Table 3.2, which lists the plastic strain, $\underline{\varepsilon}^{pl}(\eta, \underline{\dot{\varepsilon}}^{pl})$, at the onset of damage as a function of the stress triaxiality, $\eta = -\frac{p}{q}$, where p is the pressure and q is the von Mises equivalent stress, and the equivalent plastic strain rate, $\underline{\dot{\varepsilon}}^{pl}$. "All" in Table 3.2 indicates that any number within the range $-100 < \eta < 100$ can be used for

the triaxiality. The ductile failure criterion with the option of "damage evolution" was defined based on the failure displacement, $u_f = 80 \ \mu$m, from a series of parametric studies conducted in this study attempting to match the numerically obtained crack patterns using FEM with those from the results of the experiments.

The characteristic of brittleness can be applied by defining a "Tensile failure" criterion in ABAQUS/Explicit. The considered tensile failure model incorporated hydrostatic pressure to determine the dynamic spalling or a pressure cutoff (Smith 2009). According to the parametric study conducted herein, $\sigma_{cutoff} = 120$ MPa was selected, where the numerical results accurately approximated the experimental findings. Finally, these ductile and brittle failure models were used in conjunction with the option "element deletion" in ABAQUS/Explicit where the finite elements experiencing such failures were removed once either of the failure criteria was met, providing numerical stability of the nonlinear solution.

Table 3.2   Ductile damage parameters

Plastic strain, $\underline{\varepsilon}^{pl}$	Stress triaxiality, η	Strain rate, $\underline{\dot{\varepsilon}}^{pl}$ (1/s)
0.30	All	0
0.20	All	1
0.12	All	2,000
0.10	All	4,000
0.10	All	40,000

3.4   Load and Boundary Conditions

Initial velocity measured on the projectile were defined in the boundary conditions and as a predefined field. The four aluminum plates (two at the top edge and two at the bottom edge of the PMMA plate) clamping the PMMA plate were fully fixed for all three global axes, accounting for the conditions of the experiments. The initial velocity of the projectile was applied in the direction of shooting, while the initial velocities for other directions were set to zero with the assumption that the trajectory of the projectile was fixed during the impacting process.

3.5   Determination of the Finite Element Mesh

The three parts (PMMA plate, projectile, and aluminum plates) were separately meshed, Fig. 3.2, based on assigned seeds with selected element length, l_e. The projectile and aluminum plates were meshed into hexahedral-shape elements (C3D8R). Each element length was specified as 1.8 mm for the projectile and 7.5 mm for the aluminum plates. On the other hand, the element shape of the PMMA plate model was specified as tetrahedral (C3D10), which enabled cracks to propagate in arbitrary paths for more realistic crack patterns due to the projectile impact. The element sizes of the PMMA plate were determined as $l_e = 1.0$ (inside the central circle) and $l_e = 2.0$ mm (outside the central circle) to strike a balance between sufficient accuracy and computational efficiency. This selection was based on a mesh convergence study of different discretization topologies.

(a)   (b)
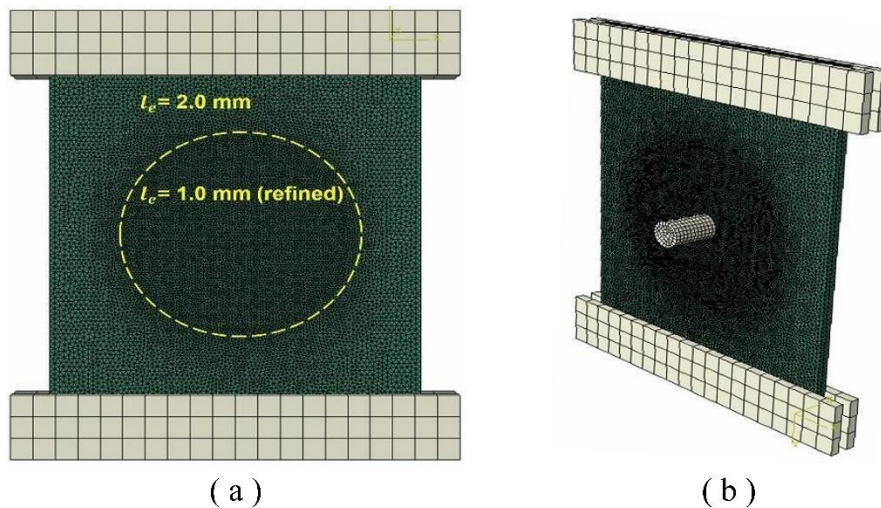
Figure 3.2   Meshed model of the PMMA plate, bullet, and aluminum target holder.

3.6   Execution of Numerical Simulations and Verification

The comparative studies were carried out based on the history outputs for energy components and projectile velocity, images of damaged plates in terms of crack propagation, perforation shape, and damaged-element distribution through the plate thickness. By comparing the results (mainly, the fracture patterns of the impacted PMMA plates) from the two approaches, the applied FEM was verified and the failure behavior for each considered case was characterized. Fig. 3.3 shows transparent PMMA plates after shootings. The results are arranged based on the plate-thickness and impact-velocity variations. In addition, Fig. 3.4 displays the FEM results of the corresponding cases from the experiments. The crack patterns had similar trends from both the experiments and the FEM regarding the variation in the size of the perforation holes, especially for the damage responses in the cases of lower impact-velocities.

Detailed comparison is shown in Fig. 3.5 for the cracked patterns of plate thickness, $h_4 = 4.5$ mm, and projectile velocity, $v_1 = 63$ m/s, case. Both tested and modeled plates were fully cracked from the impact load, and the shape of the cracked pieces matched well. Crack branching in materials especially in plate-configurations can occur due to complex stress distributions, material heterogeneity, or interactions with other pre-existing defects. In the current analysis, crack patterns are influenced by the perforating behavior, the stress state at the crack tip, and the local material properties. As illustrated in Fig. 4.1, cracks are formulated along the ductile response where radial cracks are formed with the expansion of the face while the circumferential crack occurs with the bending between free or fixed side and the central part pushed away from a bullet. The radius is dependent upon complex interaction phenomena involving the crack propagation speed, projectile size & velocity, material properties of the plate, boundary conditions, and plate thickness. The radius of the circumferential crack showed good agreement with 32 mm from the experiment and 36 mm from the simulation at the same location of the plate, i.e., difference of $\frac{(36-32)}{32} \times 100 = 12.5\%$. The difference of 12.5% is deemed acceptable due to the expected inherent uncertainty and it is concluded that the developed FEM effectively described the behavior of the experimentally studied PMMA plates.
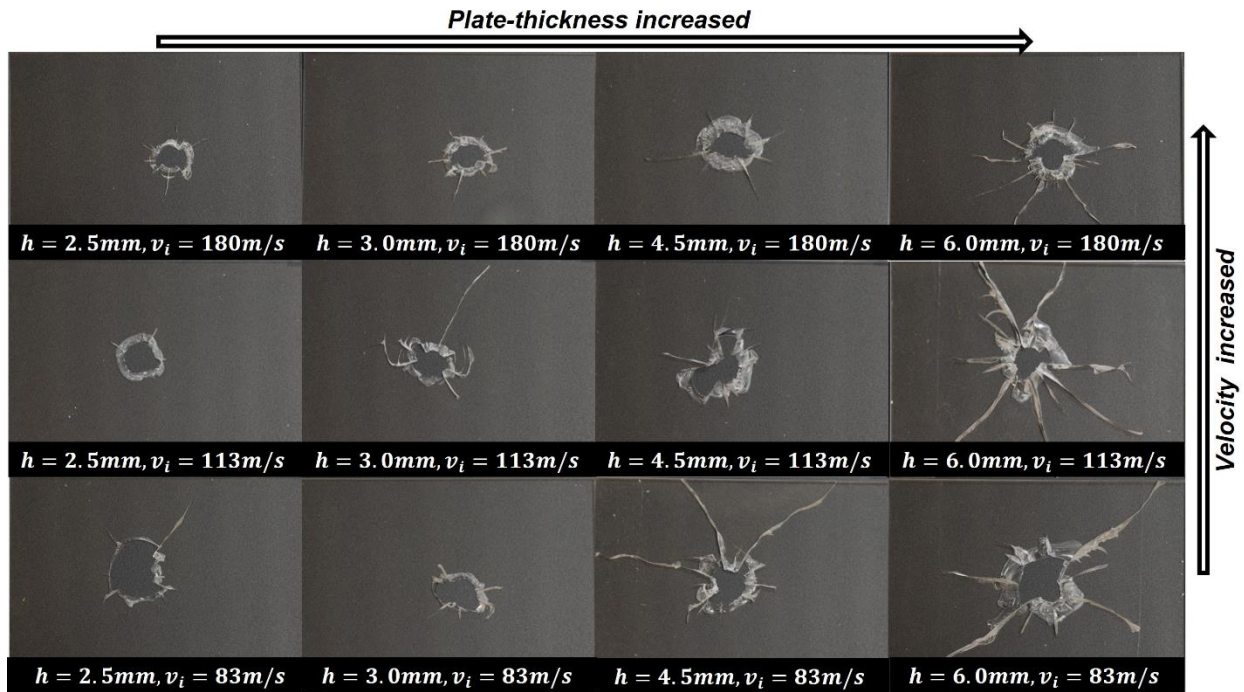
Figure 3.3 **PMMA plates after ballistic impact experiments.**
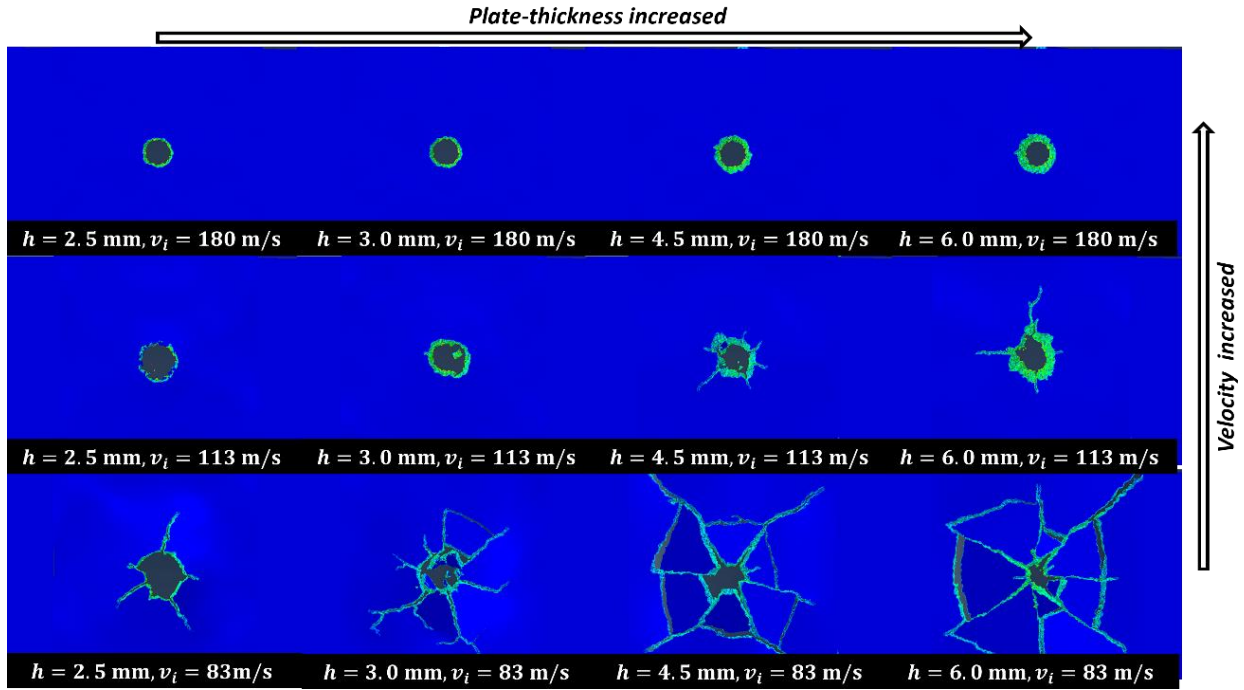
Figure 3.4   PMMA plates after ballistic impact simulations using FEM.

(a)   (b)
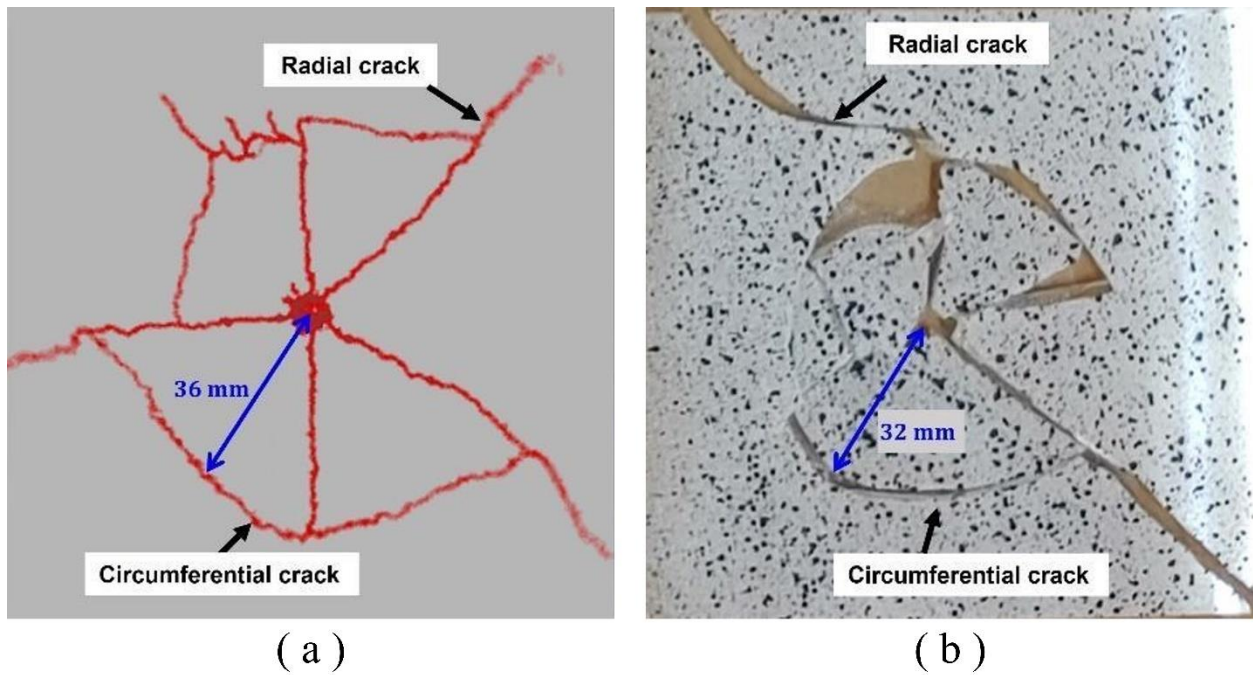
Figure 3.5   Crack comparison between experimental and FEM results from the projectile impact on $h_4 = 4.5$ mm thick plate subjected to $v_1 = 63$ m/s impact velocity.

4 Evaluation of the Damage Behavior of the PMMA Plates

4.1 Ductile to Brittle Transition

The behavior of the PMMA plate can exhibit characteristics of both brittle and ductile deformation, depending on the specific loading conditions and the material's response to the applied forces in terms of strain rate and loading configuration. The PMMA plates in Fig. 4.1 show that the PMMA plates became more brittle during the failure response with the increase of the impact velocity due to the hardening effect (Rittel and Brill 2008). The observed circumferential cracks reflected the ductile response while radial cracks were related to the brittle manifestation of the behavior. Fig. 11 shows the fracture behavior of the PMMA plate for different points in time under the impact velocity of $v_1 = 63$ m/s, Fig. 4.1(a), and $v_3 = 113$ m/s, Fig. 4.1(b), respectively representing low and high velocities. For both cases, at the time of impact between the projectile and the PMMA plate, the material experiences tensile strains due to the rapid deceleration of the projectile and the consequent stretching of the impacted surface. However, during the penetration and crushing stages, it is observed that the lower-velocity projectile causes global deformation of the plate exhibiting circumferential cracks while the higher-velocity impact cause only crushing surface around the state of pressure bounded around the impact area. This implies that larger energy is converted into internal energy and strain energy in lower-velocity impact conditions. Thus, a transition region was observed in the deformation behavior at intermediate strain rates and temperatures (not studied in this paper). In this region, the material displays a combination of both brittle and ductile characteristics, showcasing a gradual change in the failure mode as the strain rate and impact-velocity vary, which can be concluded from the energy absorption during the deformation of the impacted plates as illustrated in Fig. 4.1. Importantly, both Figs. 4.2 and 4.3 utilize the same color scale, maintain consistency in the representation of the data.

Fig. 4.2 further illustrates that circumferential cracks appeared in plates subjected to lower impact velocity due to bending of the plate from the impact, especially for plates of smaller thickness, which were indicative of the ductile behavior. On the other hand, only radial cracks extending from the center of impact towards the edges of the PMMA plates were observed for the higher impact velocity cases causing brittle failure because this higher impact velocity produced larger stress due to the hardening effect.

Fig. 4.3 represents the residual strain fields of the undeformed front view and the perforated view for four cases of the PMMA plate thickness values at $v_3 = 113$ m/s. It is noteworthy that only radial cracks occurred under relatively high velocity for all thickness cases even though the damage zone visualized with yellow color expanded with the increase of thickness explaining that the higher energy consumed.

15
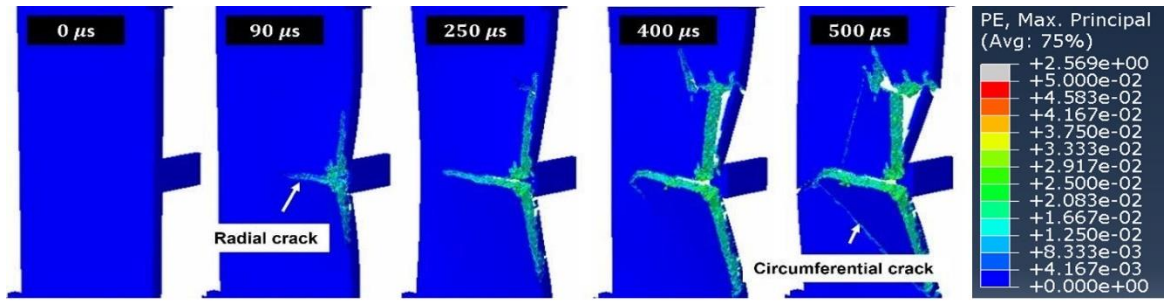
(a)
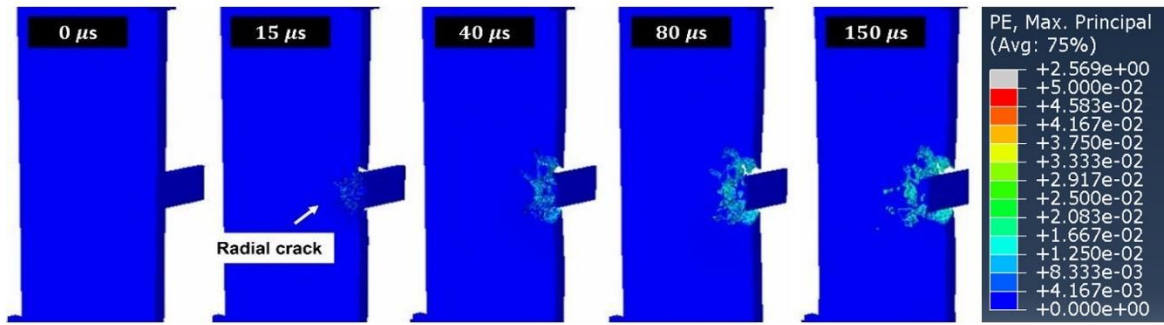
(b)

Figure 4.1   Penetration of $h_4 = 4.5$ mm thick plate subject to two different impact velocities.
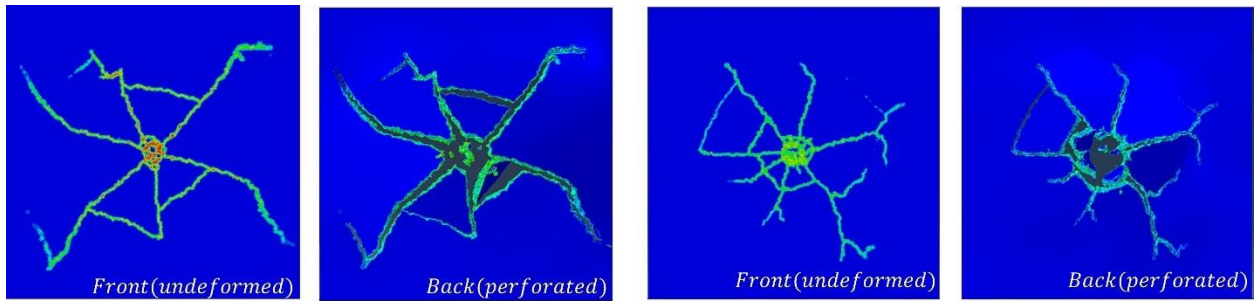
(a)

(b)
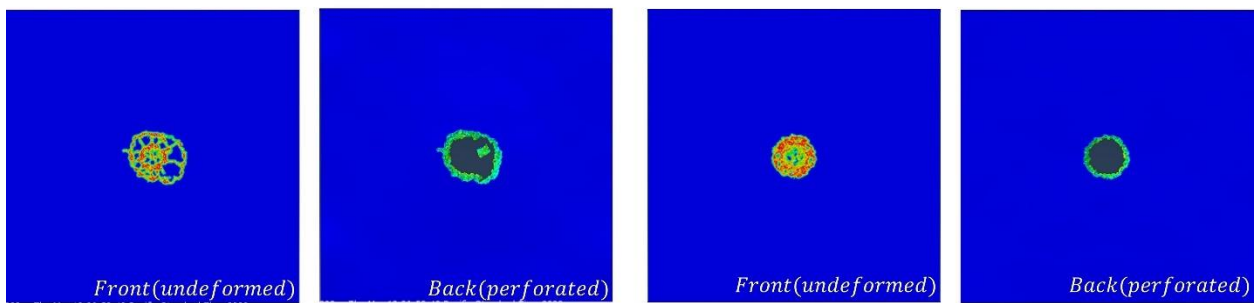
(c)

(d)

Figure 4.2 **Strain distribution fields of the undeformed front (initial contact with projectile) view and perforation results for each velocity cases at $h_3 = 3.0$ mm.**

(a)   (b)

(c)   (d)
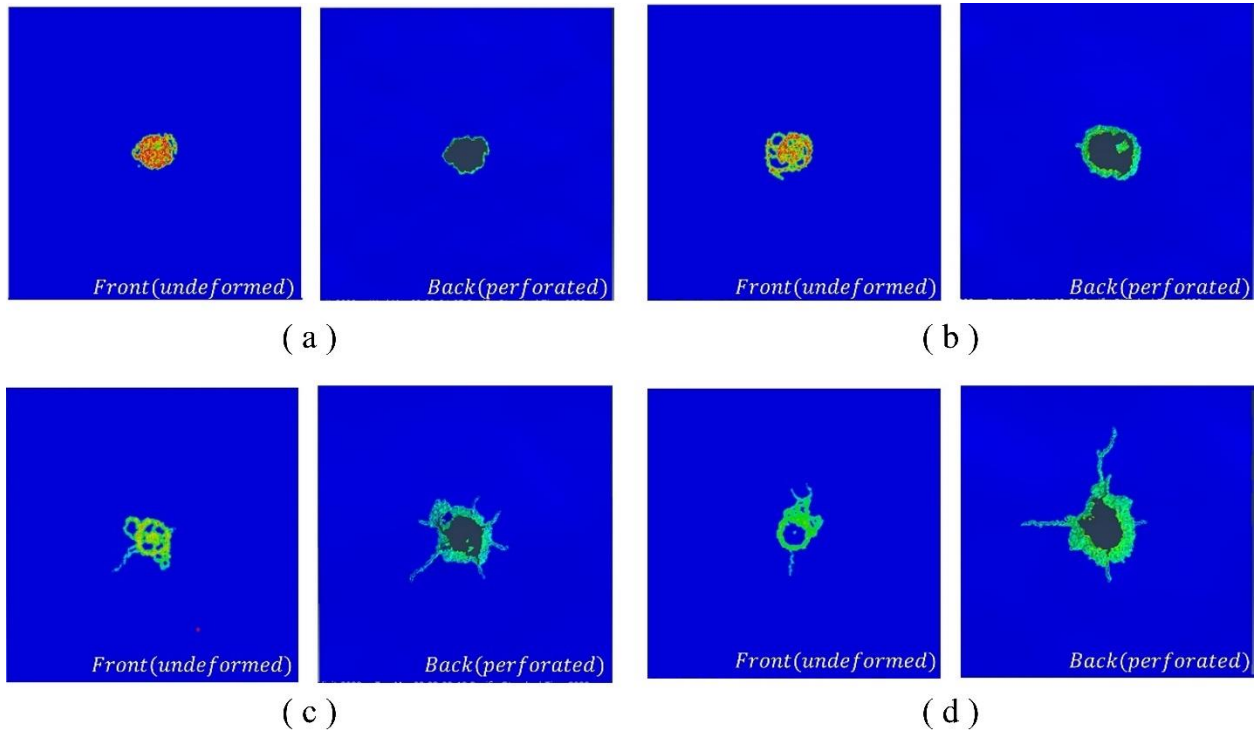
Figure 4.3 **Strain distribution fields of the undeformed front (initial contact with projectile) view and perforation results for each thickness cases at $v_3 = 113$ m/s.**

4.2   Energy Conversion During Ballistic Impact

ABAQUS/Explicit offers various energy components as the history outputs to consider in studying the energy balance (Smith 2009). The notations for the categorized energy types are as follows, E_K : Kinetic energy of the model, E_{WF} : Work done by external forces and contact friction forces, E_I : Internal energy, E_S : Elastic strain energy, E_P : Plastic dissipation energy, E_C : Energy dissipated by creep, and E_V : Energy dissipated by viscous effects.

The first law of thermodynamics implies the conservation of the total energy in the closed system where only energy components are converted to one another. Eq. (1) states the basic energy balance law where the sum of the kinetic energy for a body of volume V and mass density ρ subjected to velocity v, E_K defined in Eq. (2), and the whole internal energy, E_U, remains constant after the consumption of the external work done. Note that superposed dot implies time, t, derivative.

$$E_K + E_U - \int_0^t \dot{E}_{WF} d\tau = Constant \tag{4.1}$$

$$E_K = \int_V \frac{1}{2} \rho v \cdot v dV \tag{4.2}$$

The whole internal energy increases with the deformation of the material and is decomposed as follows,

$$E_U = \int_0^t \left(\int_V \boldsymbol{\sigma} : \dot{\boldsymbol{\varepsilon}}\, dV \right) d\tau = \int_0^t \left(\int_V \boldsymbol{\sigma^c} : \dot{\boldsymbol{\varepsilon}}\, dV \right) d\tau + \int_0^t \left(\int_V \boldsymbol{\sigma^v} : \dot{\boldsymbol{\varepsilon}}\, dV \right) d\tau = E_I + E_V \tag{4.3}$$

Decomposing the stress tensor $\boldsymbol{\sigma}$ into $\boldsymbol{\sigma}^c + \boldsymbol{\sigma}^v$ accounts for the stress from the defined constitutive law, $\boldsymbol{\sigma}^c$, and that from the viscous dissipation, $\boldsymbol{\sigma}^v$. The defined internal energy, E_I, after separating the viscous dissipation energy, E_V, is again decomposed as follows,

$$E_I = \int_0^t \left(\int_V \boldsymbol{\sigma^c} : \dot{\boldsymbol{\varepsilon}}\, dV \right) d\tau = \int_0^t \left(\int_V \boldsymbol{\sigma^c} : \dot{\boldsymbol{\varepsilon}}^{el}\, dV \right) d\tau + \int_0^t \left(\int_V \boldsymbol{\sigma^c} : \dot{\boldsymbol{\varepsilon}}^{pl} dV \right) d\tau +$$
$$\int_0^t \left(\int_V \boldsymbol{\sigma^c} : \dot{\boldsymbol{\varepsilon}}^{cr} dV \right) d\tau \; = E_S + E_P + E_C \tag{4.4}$$

Introducing the decomposition of the strain rate tensor, $\dot{\boldsymbol{\varepsilon}} = \dot{\boldsymbol{\varepsilon}}^{el} + \dot{\boldsymbol{\varepsilon}}^{pl} + \dot{\boldsymbol{\varepsilon}}^{cr}$, where the strain rate values are divided into the components of elastic, plastic, and creep strain rates, respectively. Finally, E_S implies the elastic-strain energy, E_P is the plastic-strain energy, which accounts for the plastic dissipation energy, and E_C corresponds to the energy dissipation by deformations due to creep or swelling. The energy terms can be exported from the numerical results in the form of time-history for the purpose of quantitative comparisons of the studied cases of the PMMA plates.

Fig. 4.4 shows the time histories of the kinetic, E_K, Internal, E_I , strain, E_S, and plastic dissipation, E_P, energy components for various impact-velocity values. Each energy component history is shown in two versions:

1) Normalized by maximum kinetic energy from v_1 case, Table 2.2, i.e., $E_{component}/E_{K,v_1}^{max}$.

2) Normalized by respective maximum kinetic energy for $v_i, i = 1, \cdots ,5$, i.e., $E_{component}/E_{K,v_i}^{max}$.

The histories of the second version are referred to as "normalized" where the comparison is more transparent. The initial kinetic energy originating from the projectile-velocity slightly decreased and was converted into internal energy, involving strain energy and dissipation energy, Figs. 4.4(a) and (b). Moreover, the normalized kinetic energy loss was inversely proportional to the impact velocity, Fig. 4.4(b). In contrast, the energy conversion into the strain and internal energy occurred the most for the lowest velocity case, Figs. 4.4(c) to (f). It is to be noted that the proportion of energy converted into internal energy was negligible in cases above a certain projectile-velocity, Fig. 4.4(c), where less than 5% of the initial kinetic energy was converted to internal energy in v_3 to v_5 cases, Fig. 4.4(d), during the impact. This result implied that the elements directly under the high-speed-impact failed early through the thickness before the stress waves propagated in the in-plane directions, which hardly led to the deformation of the material near the directly impacted area. On the other hand, Figs. 4.4(g) and (h) suggest that the resulting plastic dissipation energy histories had a different trend from the other energy components. Whereas the plastic dissipation

also decreased with the higher velocities, in general, due to global fracturing behavior, this component was larger for the three high-velocity cases, namely, v_3 to v_5. It is reasonable to expect that the abrupt and high magnitude of impact locally caused extreme plastic strain to the elements in the center of the plate resulting in this directly proportional trend between the plastic dissipation energy and the impact-velocity for these three cases.

The energy history studies from the numerical results offer insights into how the initial kinetic energy of the projectile was converted and consumed during the impact. The reduced kinetic energy was converted into various components such as that due to elastic deformation and plastic dissipation of the target with different ratios, depending on the impact-velocity, but keeping the total energy reduction unchanged despite of the varying velocity, as shown in Fig. 4.4(a). Even though the variation in the impact-velocity caused different deformations and the crack pattern behavior, the kinetic energy loss of the projectile (bullet) was independent from these factors. The same degree of energy loss for each velocity case decreased the normalized kinetic energy of lower-velocity cases more drastically as shown in Fig. 4.4(b). Moreover, it is concluded that the energy loss from the impact is mainly comprised of the strain energy which accounts for the energy consumption due to deformation of the target. Since the higher velocity case tends to have more brittle behavior of the plates under impact, leading to a rapid loss of resistance during the impact, the higher velocity impact hardly generated internal or strain energy quantities, Figs. 4.4(c) and (e).
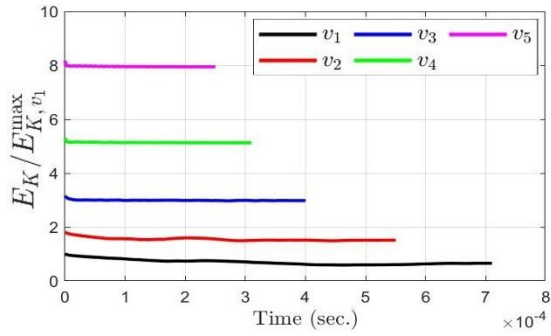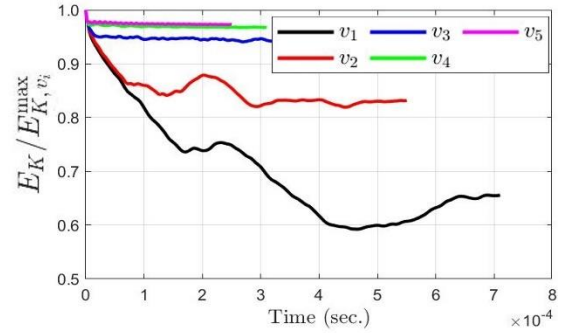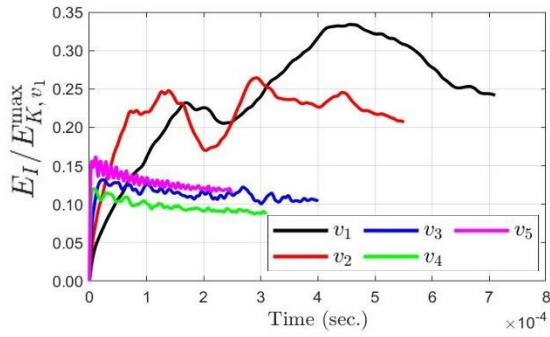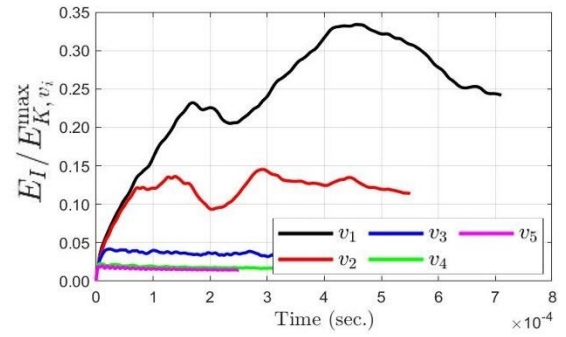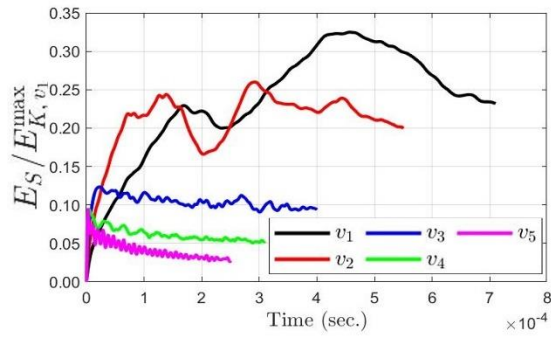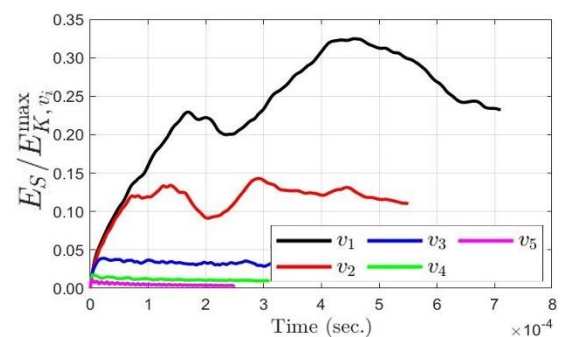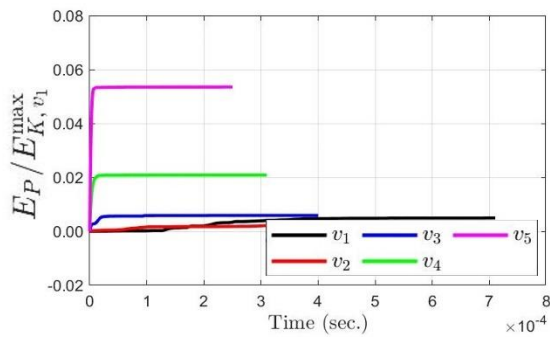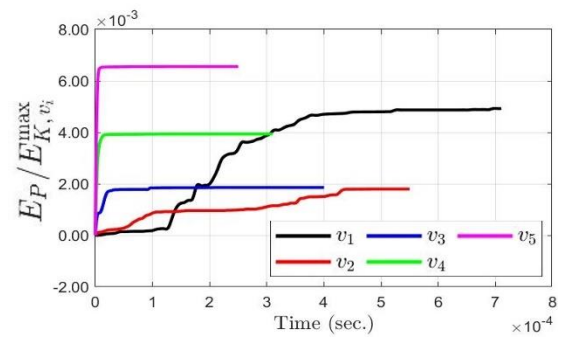
Figure 4.4   Energy histories from different initial velocity of the projectile for $h_3 = 3.0$ mm.

4.3 Energy Absorption by Projectile-Impact

Considering the projectile (p) after impact and using the performed 25 simulations of all considered cases in the experiments with varying PMMA plate thicknesses and impact velocities, Fig. 4.5(a) shows the residual velocity, v_r, plotted against its initial velocity, v_i, for the different cases. Similarly, Fig. 4.5(b) shows the residual normalized kinetic energy, $E_{K,r}^{*(p)} = E_{K,r}^{(p)}/E_{K,r}^{(p)}(v_1)$, plotted against its initial counterpart, $E_{K,i}^{*(p)} = E_{K,i}^{(p)}/E_{K,i}^{(p)}(v_1)$, for the same cases. It is noted that the kinetic energy of the projectile is calculated from $E_K^{(p)} = \frac{1}{2}m_p v_p^2$, where m_p and v_p are respectively the mass and velocity of the projectile. As expected, the projectile velocity plots, Fig. 4.5(a), become close to the baseline with the smaller impacted plate-thickness. Moreover, the thicker the plate, the less linear the plots, which is especially noticeable for $h_4 = 4.5$ mm and $h_5 = 6.0$ mm models. On the other hand, the projectile kinetic energy plots, Fig. 4.5(b), are almost linear and parallel for all thickness cases. These observations indicate that the change of the projectile kinetic behavior from the impact is attributed to the energy loss due to reduced velocity by the impact. Fig. 4.6 displays the reduction of velocity and kinetic energy of the projectile (bullet) from the impact for different plate thicknesses and initial impact velocities. Fig. 4.6(a) shows that the projectile loses its velocity more drastically from the impact on thicker plates when its velocity is lower than a specific value, 113 m/s, in the present study. On the other hand, Fig. 4.6(b) implies that the kinetic energy loss of the projectile does not strongly depend on the impact velocity, whereas the lost kinetic energy increases linearly with the plate thickness. These remarks suggest that the velocity reduction of the projectile originates from the energy conversion, which linearly increases with the plate-thickness while the impact velocity slightly affects the amount of this reduction. This conclusion suggests that the thickness of a PMMA plate, used as a protective armor, can be designed simply in advance to only satisfy the requirements to absorb the expected impact energy without considering the complex mechanism during the impact itself.
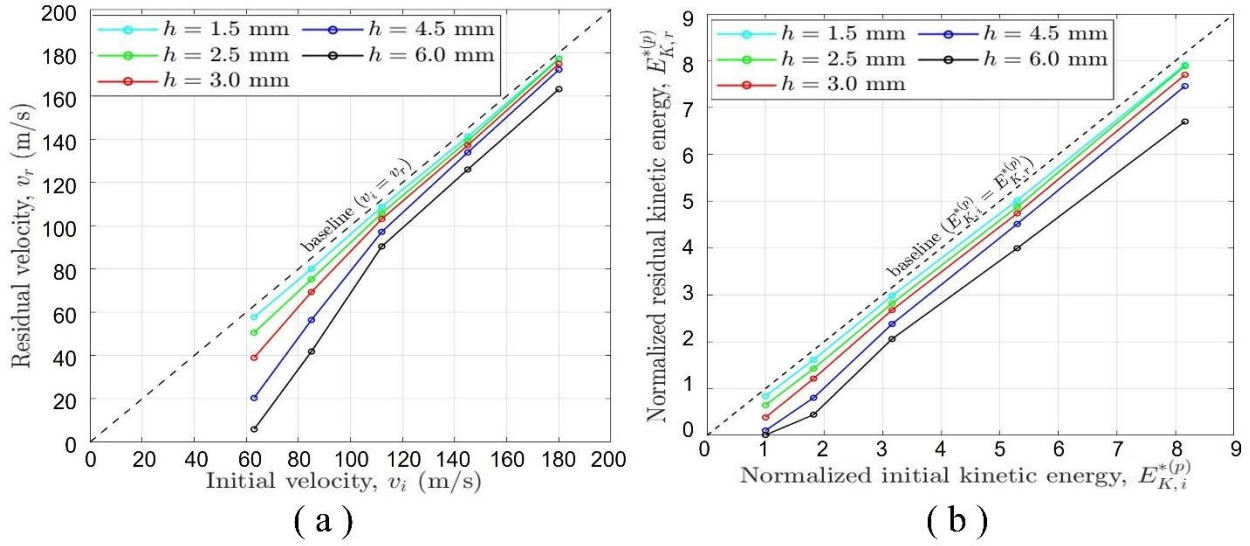
Figure 4.5   Initial vs. residual velocity and kinetic energy of the projectile.
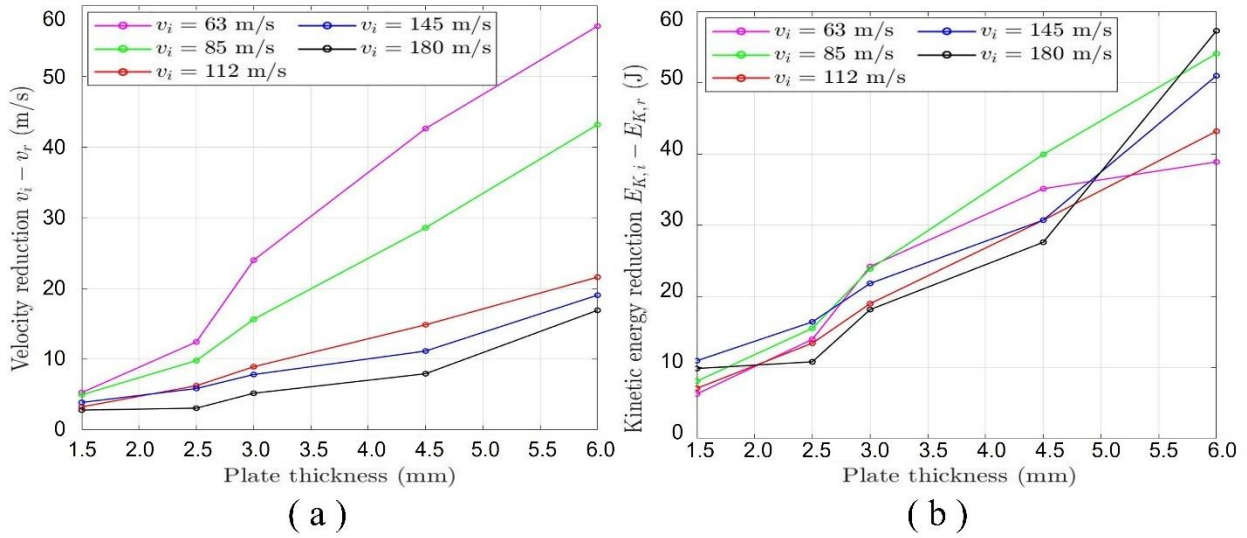
Figure 4.6   Velocity and kinetic energy reduction from impact of the projectile.

5   Conclusions

Ballistic impact experiments and numerical simulations using the FEM are conducted on PMMA plates of different thickness and impact-velocity. These plates can be an effective solution for protective shields. Moreover, if they are used for their transparent properties, they supersede glass in terms of mechanical behavior. Both experiments and simulations using the FEM are conducted on five plate-thickness cases for five impact-velocity values for a total of 25 studied cases. The crack patterns and perforations from each case during the experiments and simulations are compared verifying the computational models using the FEM. The main conclusions can be summarized as follow:

- The ductile and tensile failure criteria considered in the FEM of the PMMA plate produced reasonable approximation to the experimental results throughout all considered cases with different plate-thicknesses and impact-velocity values.

- The experimental and numerical results show that the PMMA plates become more brittle under the higher impact-velocity due to the rate-dependency and hardening effect.

- The numerical approach using FEM offers considerable insight into the energy conversion during ballistic impact, and dependency of the damage behavior of the PMMA plate on the plate thickness and the projectile-velocity.

- From the numerical simulations, it is observed that the kinetic energy loss of the projectile during the impact is linearly varying with the plate-thickness regardless of the initial velocity of the projectile (bullet).

The energy conversion of PMMA can be further studied with the quantification of experimental results, such as 3D-DIC analysis and the investigation of residual velocity of bullet after impact to estimate the out-of-plane deformation and ballistic limit, respectively. The continued investigation of PMMA with the numerical approach would establish future usage for PMMA to be a more suitable material substituting glass.

References

Barthes, Clément. OpteCAL. Accessed January 20, 2022. https://optecal.com/.

Bless, Stephan, Bobby Peden, Ivan Guzman, Mehdi Omidvar, and Magued Iskander. (2018). Dynamic Behavior of Materials, Volume 1. 1 (January): 373–80. https://doi.org/10.1007/978-3-319-62956-8.

CAE Abaqus. (2009). Version 6. In Dassault Systemes, RI, USA.

Dong, Yongxiang, Shunshan Feng, Guangyan Huang, Chunmei Liu, Lixing Xiao, and Qing Song. (2012). Ballistic Impact Characteristics of Flat-Nose Projectile Penetrating Concrete and Soil Compound Target. International Journal of Nonlinear *Sciences and Numerical Simulation* 13 (3–4): 255–60. https://doi.org/10.1515/ijnsns-2011-0144.

Dorogoy, A., and D. Rittel. (2014). Impact of Thick PMMA Plates by Long Projectiles at Low Velocities. Part II: Effect of Confinement." *Mechanics of Materials* 70: 53–66. https://doi.org/10.1016/j.mechmat.2013.11.009.

Dorogoy, A., D. Rittel, and A. Brill. (2010). A Study of Inclined Impact in Polymethylmethacrylate Plates. *International Journal of Impact Engineering* 37 (3): 285–94. https://doi.org/10.1016/j.ijimpeng.2009.06.013.

Gama, Bazle A., Sergey L. Lopatnikov, and John W. Gillespie. (2004). Hopkinson Bar Experimental Technique: A Critical Review. *Applied Mechanics Reviews* 57 (1–6): 223–50. https://doi.org/10.1115/1.1704626.

Gee, Bruce, Matin Parchei-Esfahani, and Robert Gracie. (2020). XFEM Simulation of a Mixed-Mode Fracture Experiment in PMMA. *Engineering Fracture Mechanics* 229 (December 2019): 106945. https://doi.org/10.1016/j.engfracmech.2020.106945.

Hanifehzadeh, Mohammad, and Mir Mohammad Reza Mousavi. (2019). Predicting the Structural Performance of Sandwich Concrete Panels Subjected To Blast Load Considering Dynamic Increase Factor. *Journal of Civil Engineering, Science and Technology* 10 (1): 45–58. https://doi.org/10.33736/jcest.1067.2019.

Hibbit, Karlson, and Sorensen. (1998). *ABAQUS/Explicit: User's Manual*. Vol. 1.

Hsieh J., Alex, Daniel DeSchepper, Paul Moy, Peter Dehmer G., and John Song W. (2004). The Effects of PMMA on Ballistic Impact Performance of Hybrid Hard/Ductile All-Plastic- and Glass-Plastic-Based Composites. *Army Research Laboratory*, no. February. http://stinet.dtic.mil/oai/oai?&verb=getRecord&metadataPrefix=html&identifier=ADA420878.

Jiang, Fengchun, and Kenneth S. Vecchio. (2009). Hopkinson Bar Loaded Fracture Experimental Technique: A Critical Review of Dynamic Fracture Toughness Tests. *Applied Mechanics Reviews* 62 (6): 1–39. https://doi.org/10.1115/1.3124647.

Kajisa, Taira, Haruko Miyauchi, Kazumi Mizuhara, Kentaro Hayashi, Tooru Tokimitsu, Masanao Inoue, Kohjiro Hara, and Atsushi Masuda. (2014). Novel Lighter Weight Crystalline Silicon Photovoltaic Module Using Acrylic-Film as a Cover Sheet. *Japanese Journal of Applied Physics* 53 (9). https://doi.org/10.7567/JJAP.53.092302.

Kueh, A. B.H., and Y. Y. Siaw. (2021). Impact Resistance of Bio-Inspired Sandwich Beam with Side-Arched and Honeycomb Dual-Core. *Composite Structures* 275 (April): 114439. https://doi.org/10.1016/j.compstruct.2021.114439.

Martins, Ana C., Valentin Chapuis, Fanny Sculati-Meillaud, Alessandro Virtuani, and Christophe Ballif. (2018). Light and Durable: Composite Structures for Building-Integrated Photovoltaic Modules. *Progress in Photovoltaics: Research and Applications* 26 (9): 718–29. https://doi.org/10.1002/pip.3009.

Ogihara, Shinji, Tomoyuki Ishigure, and Akira Kobayashi. (1998). Study on Impact Perforation Fracture Mechanism in PMMA. *Journal of Materials Science Letters* 17 (8): 691–92. https://doi.org/10.1023/A:1006653231432.

Pan, Bing. (2018). Digital Image Correlation for Surface Deformation Measurement: Historical Developments, Recent Advances and Future Goals. *Measurement Science and Technology* 29 (8). https://doi.org/10.1088/1361-6501/aac55b.

Patel, PJ, AJ Hsieh, and GA Gilde. (2006). Improved Low-Cost Multi-Hit Transparent Armor. *Army Research Lab Aberdeen Proving Ground MD Weapons and Materials Research Directorate*. http://oai.dtic.mil/oai/oai?verb=getRecord&metadataPrefix=html&identifier=ADA481074.

Pawar, Eshwar. (2016). Related Papers St Rength Appraisal of Fibre Reinforced Concrete with Part Ial Replacement of OPC With Miner… A Review Article on Acrylic PMMA. *IOSR Journal of Mechanical and Civil Engineering (IOSR-JMCE) e-ISSN* 13 (2): 1–04. https://doi.org/10.9790/1684-1302010104.

Pereira, L. F., J. Weerheijm, and L. J. Sluys. (2018). Simulation of Compaction and Crushing of Concrete in Ballistic Impact with a New Damage Model. *International Journal of Impact Engineering* 111 (September 2017): 208–21. https://doi.org/10.1016/j.ijimpeng.2017.09.014

Petrudi, Amin Moslemi, Khodadad Vahedi, Masoud Rahmani, and Mohammadali Moslemi Petrudi. (2020). Numerical and Analytical Simulation of Ballistic Projectile Penetration Due to High Velocity Impact on Ceramic Target. *Frattura Ed Integrita Strutturale* 14 (54): 226–48. https://doi.org/10.3221/IGF-ESIS.54.17.

Rittel, D., and A. Brill. (2008). Dynamic Flow and Failure of Confined Polymethylmethacrylate. *Journal of the Mechanics and Physics of Solids* 56 (4): 1401–16. https://doi.org/10.1016/j.jmps.2007.09.003.

Rittel, D., and A. Dorogoy. (2008). A Methodology to Assess the Rate and Pressure Sensitivity of Polymers over a Wide Range of Strain Rates. *Journal of the Mechanics and Physics of Solids* 56 (11): 3191–3205. https://doi.org/10.1016/j.jmps.2008.08.001.

Sarva, Sai, Adam D. Mulliken, Mary C. Boyce, and Alex J. Hsieh. (2006). Mechanics of Transparent Polymeric Material Assemblies Under Projectile Impact: Simulations and Experiments, 227–34. https://doi.org/10.1142/9789812772572_0029.

Scari, Alexandre da Silva, Bruno Cesar Pockszevnicki, Jánes Landre Junior, and Pedro Americo Almeida Magalhaes Junior. (2014). Stress-Strain Compression of AA6082-T6 Aluminum Alloy at Room Temperature. *Journal of Structures* 2014: 1–7. https://doi.org/10.1155/2014/387680.

Smith, Michael. (2009). *ABAQUS/Standard User's Manual*. Version 6. English. United States: Dassault Systemes Simulia Corp.

Tekalur, Srinivasan Arjun, Wei Zhang, and Luan Huynh. (2010). Dynamic Failure of Monolithic and Layered PMMA and PC Plates. *Implast* 1: 93–104. https://doi.org/10.1007/978-1-4419-8228-5.

Zahid, Muhammad Aleem, Hyeongsik Park, Young Hyun Cho, and Junsin Yi. (2021). Plasma Etched PMMA/CaF2 Anti-Reflection Coating for Light Weight PV Module. *Optical Materials* 112 (October 2020): 110813. https://doi.org/10.1016/j.optmat.2021.110813.

Zhang, Jianjun, Tao Jin, Zhihua Wang, and Longmao Zhao. (2016). Experimental Investigation on Yield Behavior of PMMA under Combined Shear-Compression Loading. *Results in Physics* 6: 265–69. https://doi.org/10.1016/j.rinp.2016.05.004.

Zhou, Zhiwei, Buyun Su, Zhihua Wang, Zhiqiang Li, Xuefeng Shu, and Longmao Zhao. (2013). Shear-Compression Failure Behavior of PMMA at Different Loading Rates. *Materials Letters* 109: 151–53. https://doi.org/10.1016/j.matlet.2013.05.081.

The Pacific Earthquake Engineering Research Center (PEER) is a multi-institutional research and education center with headquarters at the University of California, Berkeley. Investigators from over 20 universities, several consulting companies, and researchers at various state and federal government agencies contribute to research programs focused on performance-based earthquake engineering.

These research programs aim to identify and reduce the risks from major earthquakes to life safety and to the economy by including research in a wide variety of disciplines including structural and geotechnical engineering, geology/ seismology, lifelines, transportation, architecture, economics, risk management, and public policy.

PEER is supported by federal, state, local, and regional agencies, together with industry partners.

PEER Core Institutions

University of California, Berkeley (Lead Institution)
California Institute of Technology
Oregon State University
Stanford University
University of California, Davis
University of California, Irvine
University of California, Los Angeles
University of California, San Diego
University of Nevada, Reno
University of Southern California
University of Washington